

# The soft impact response of composite laminate beams

Karthikeyan K.<sup>1</sup>, B. P. Russell<sup>1</sup>, N.A. Fleck,<sup>1</sup> M. O'Masta<sup>2</sup> and H.N.G. Wadley<sup>2</sup> and  
V.S. Deshpande<sup>1</sup>

<sup>1</sup>Cambridge University Engineering Department, Trumpington Street, Cambridge CB2 1PZ, UK.

<sup>2</sup>Department of Material Science & Engineering,  
School of Engineering and Applied Science, University of Virginia, Charlottesville, VA 22903, USA.

## Abstract

The quasi-static and dynamic responses of laminated beams of equal areal mass, made from monolithic CFRP and Ultra high molecular weight Polyethylene (UHMWPE), have been measured. The end-clamped beams were impacted at mid-span by metal foam projectiles to simulate localised blast loading. The effect of clamping geometry on the response was investigated by comparing the response of beams bolted into the supports with the response of beams whose ends were wrapped around the supports. The effect of laminate shear strength upon the static and dynamic responses was investigated by testing two grades of each of the CFRP and UHMWPE beams: (i) CFRP beams with a cured matrix and uncured matrix, and (ii) UHMWPE laminates with matrices of two different shear strengths. Quasi-static stretch-bend tests indicated that the load carrying capacity of the UHMWPE beams exceeds that of the CFRP beams, increases with diminishing shear strength of matrix, and increases when the ends are wrapped rather than through-bolted. The dynamic deformation mode of the beams is qualitatively different from that observed in the quasi-static stretch-bend tests. In the dynamic case, travelling hinges emanate from the impact location and propagate towards the supports; the beams finally fail by tensile fibre fracture at the supports. The UHMWPE beams outperform the CFRP beams in terms of a lower mid-span deflection for a given impulse, and a higher failure impulse. Also, the maximum attainable impulse increases with decreasing shear strength for both the UHMWPE and CFRP beams. The ranking of the beams for load-carrying capacity in the quasi-static stretch-bend tests is identical to that for failure impulse in the impact tests. Thus, the static tests can be used to gauge the relative dynamic performances of the beams.

Keywords: *beams, blast loading, foam projectile, armour, UHMWPE laminates*

## 1. Introduction

Ultra High Molecular Weight Polyethylene (UHMWPE) fibres were commercialised in the late 1970s by DSM Dyneema, NL under the trade name *Dyneema*<sup>®</sup> and more recently by Honeywell in the USA under the trade name *Spectra*. Both materials have densities of  $\rho_f = 970 \text{ kgm}^{-3}$  below that of water and tensile strengths in excess of 3 GPa [1]. The very high specific strength of these fibres has led to many applications in high performance sails, fishing lines, marine mooring cables; in laminate form they are used for ballistic protection [2-3] and in woven-fabric form for protective gloves.

A number of studies have been conducted to measure the static [4-12] and dynamic response [13-17] of UHMWPE fibres and composites. For example, Russell et al. [18] have explored the highly anisotropic nature of UHMWPE composites: they measured tensile strengths of a few GPa along the fibre direction, and an in-plane shear strength of less than 10 MPa. Moreover, they observed that UHMWPE fibres display nearly no strain rate sensitivity for strain rates up to about  $10^3 \text{ s}^{-1}$ . Such measurements are used to develop continuum models (Grujicic et al. [19, 20], Iannucci and Pope [21]) and are implemented within finite element codes in order to model the penetration resistance of UHMWPE composites.

Recently, there has been considerable interest in the application of multi-layered UHMWPE laminated composites to enhance the ballistic resistance of light weight vehicles. This interest arises from a commonly held view that the ballistic limit of fibre composites scales linearly with the so-called Cunniff velocity  $c^*$  of the fibre as given by

$$c^* = \left( \frac{\sigma_f \varepsilon_f}{2\rho_f} \sqrt{\frac{E_f}{\rho_f}} \right)^{1/3} \quad (1.1)$$

where  $\sigma_f$  and  $\varepsilon_f$  are tensile failure strength and strain of the fibres, respectively, while  $E_f$  is the tensile modulus of the fibres. The ballistic performance of a large number of fibre composite systems scale with  $c^*$ , see Cunniff [2]. Subsequently, Phoenix and Porwal [3] rationalised this theoretically via a dynamic membrane stretching model. Candidate ballistic materials are plotted in Fig. 1 using axes of specific energy absorption and longitudinal wave speed. Contours of constant Cunniff velocity  $c^*$  are included in this plot. It is clear by this

metric that the various grades *Dyneema*<sup>®</sup> fibre (SK60, SK76 etc.) and *Spectra* considerably outperform most other fibres and also surpass armour steels, supporting their use in ballistic applications. In contrast to the use of UHMWPE laminated composites for ballistic application, little data have been published on the ability of these composites to withstand air blast or landmine blast.

There is considerable current interest in the development of an understanding for the response of UHMWPE composite structures subjected to landmine blast loading; this is the focus of the present paper. Detailed dynamic measurements and observations of the deformations via high speed photography are difficult in experiments involving the detonation of explosives (the gaseous explosive products often engulf the test structure and obscure visualisation via standard high speed photography). Thus, alternative methods to simulate landmine blast loading within a laboratory setting have been proposed.

[Park et al. \[22\]](#) have developed an apparatus to launch high speed sand slugs against structures to simulate the localised loading of structures by ejecta from a landmine explosion. They have demonstrated that the loading due to the sand is primarily inertial in nature. While such experiments conducted with sand slugs provide significant information on the mechanisms of the interaction of structure with sand ejecta, they are very difficult to perform and it is not practical to use this method for a wide ranging experimental study. More recently, [Liu et al. \[23\]](#) have used coupled discrete-continuum calculations to show that a metal foam projectile is able to simulate the loading of a sand slug to a remarkable degree of accuracy. The dynamic loading of structures via foam projectiles was first introduced by [Radford et al. \[24\]](#) as a method to simulate the soft impact of structures. Subsequently, this method has been widely used to quantify the dynamic performance of range of monolithic metal and sandwich structures [\[25-28\]](#) and was recently employed by [Russell et al. \[29\]](#) to study the dynamic response of Carbon Fibre Reinforced Plastic (CFRP) monolithic and sandwich beams.

The present study investigates the dynamic response of UHMWPE beams subject to sand ejecta loading as simulated via a metal foam projectile impact, and compares the response of UHMWPE and CFRP composite beams. We restrict attention to UHMWPE laminates with

an equal number of 0° and 90° plies: such laminates are the most commonly used layup of UHMWPE laminates for ballistic application. The focus is on understanding the effect of the matrix properties and of end clamping geometry on the blast performance of these structures.

The outline of our study is as follows. We first report the manufacture of two grades of UHMWPE and CFRP composites and their quasi-static material properties. Next, we discuss the quasi-static stretch-bend response of beams made from these composites. Finally, the dynamic response of these beams subject to a metal foam impact is reported and the dynamic and quasi-static deformation and failure mechanisms contrasted. These observations are used to rationalise a method to rank the relative dynamic performance of the different beams using only quasi-static measurements.

## 2. Materials and properties

Two types of fibre laminates were investigated: (i) UHMWPE laminates manufactured by DSM Dyneema<sup>1</sup> and (ii) CFRP laminates manufactured by Hexcel Composites<sup>2</sup>. Two variants of each of these composites were employed in this study and their designations, fibre and matrix types, lay-ups and volume fraction  $V_f$  of fibres are listed in [Table 1](#). All composite plates had an areal mass of approximately  $5.89 \text{ kg m}^{-2}$  with plate thicknesses as indicated in [Table 1](#). A brief description of the manufacturing route for each of these composites is given below.

### 2.1 Composite fabrication

*DSM Dyneema composites.* Two grades of laminate, with commercial designations HB26 and HB50, were employed. The two laminates contained different matrices, and had slightly different number of plies in order to give the same areal mass, as detailed in [Table 1](#). Both laminates are manufactured in 3 steps:

---

<sup>1</sup> DSM Dyneema, NL.

<sup>2</sup> Hexcel Composites, Duxford, UK.

Step I: Fibres are produced through a gel-spinning/hot drawing process [30,31]. The UHMWPE is dissolved in a solvent at a temperature of 150°C and the solution is pumped through a spinneret comprising a few hundred capillaries to form liquid filaments. These liquid filaments are then quenched in water to form a gel-fibre. The gel-fibre is drawn at a strain rate on the order of  $1 \text{ s}^{-1}$  in hot air (at 120°C), resulting in a highly orientated and highly crystalline fibre of diameter 17  $\mu\text{m}$ .

Step II: Fibres are coated in matrix resin solution and are then formed into a  $[0^\circ/90^\circ/0^\circ/90^\circ]$  stack. The stack is then dried to remove the matrix solvent.

Step III: The  $[0^\circ/90^\circ/0^\circ/90^\circ]$  stack is cut, laid-up to the required thickness and hot pressed (using a pressure of 20 MPa at 120° C). Bonding of the layers is achieved through partial melting of the matrix.

*CFRP laminates.* Hexply® 8552/33%/134/IM7 (12K) pre-preg, comprising unidirectional IM7 carbon fibres in an epoxy resin (fiberite 934), was obtained from Hexcel composites. Two composites were manufactured, with identical lay-ups as detailed in Table 1. The so-called cured composite was generated using the standard cure cycle for this resin system (2 hours at 120°C, held under a pressure of 0.6 MPa) and shall be subsequently referred to as ‘CFRP-C’. The uncured composite was used in its pre-preg state and stored at -15°C. This uncured composite shall be subsequently referred to as ‘CFRP-U’ and was thawed at room temperature for 5 hours prior to testing.

## 2.2 *Material properties*

Quasi-static material tests were performed in order to characterise some of the composite properties that dictate the response of the clamped beams investigated here. Three types of tests were performed on the  $0^\circ/90^\circ$  composites:

- (i) Uniaxial tensile tests in the  $0^\circ/90^\circ$  orientation such that the  $0^\circ$  plies were aligned with the tensile axis. The UHMWPE and the CFRP-U laminates have a high tensile

strength along the fibre directions, but possess a very low shear strength. Thus, a standard tabbed specimen geometry cannot be used to measure the stress versus strain response in the  $0^\circ/90^\circ$  orientation, as discussed by Russell et al. [18]. They designed a specimen with a large gripping area and a narrow gauge width as sketched in Fig. 2a, and we made use of this geometry for our tests on the UHMWPE laminates. The tensile tests were conducted in a screw-driven test machine at a nominal applied strain rate of  $10^{-3}\text{s}^{-1}$ . The nominal stress was determined from the load cell of the test machine, and the axial nominal strain was measured using a clip gauge of gauge length 12.5 mm. For the CFRP-C composites, tensile tests were conducted at an applied strain rate of  $10^{-3}\text{s}^{-1}$  in accordance with the ASTM standard D3039.

- (ii) Tensile tests on the composites in the  $\pm 45^\circ$  orientation were performed such that the fibres lay at  $\pm 45^\circ$  with respect to the tensile axis. While no special specimen geometries were needed we chose to use the same specimen geometries and procedure as used for the  $0^\circ/90^\circ$  tensile tests.
- (iii) Double-notch shear tests were used to measure the inter-laminar shear response, Fig. 2b. These tests were conducted using a double-notch specimen geometry [32,33] with appropriate modifications. Specifically, strips of length 150 mm, width  $b = 20$  mm and thickness  $h = 6$  mm were cut from the UHMWPE and the uncured CFRP sheets. Inter-laminar shear was promoted over a gauge length of length  $l = 30$  mm by drilling one hole and 2 notches over the central section of the specimen as sketched in Fig. 2b. Care was taken to ensure that the hole/notches were positioned so that there were no continuous fibres that spanned the entire length of the specimen. The tests were conducted by friction gripping the specimen ends and pulling them as indicated in Fig. 2b in a screw driven test machine. The inter-laminar shear stress  $\tau_{31}$  was defined as  $\tau_{31} \equiv P/(2lb)$ , where  $P$  is the measured tensile load and the factor of 2 was introduced as shear occurs over 2 inter-laminar planes as shown in Fig. 2b. The shear displacements was measured by mounting a clip gauge on either side of the notch, as indicated in Fig. 2b. These tests were conducted at a low and high applied displacement rate of 1 mm/min and 500 mm/min, respectively. Although we measured the inter-laminar shear

properties of the HB26, HB50 and CFRP-U composites, double notch shear tests results are not reported for the CFRP-C composites. The CFRP-C composites have a high shear strength and the double-notch specimen resulted in a mode-II fracture of the specimen and hence was not suitable to extract the inter-laminar shear stress versus displacement response. However, the interlaminar shear strength of the 0°CFRP-C composites equals 120 MPa according to the Hexcel data sheet for this material.<sup>3</sup>

The tensile stress versus strain curves of the UHMWPE and CFRP laminates in the 0° / 90° orientation are plotted in Fig. 3a for an applied strain rate of 10<sup>-3</sup>s<sup>-1</sup>. In this orientation, all four composites display an approximately elastic-brittle response, with the response dictated by the fibres. Hence, the HB26 and HB50 UHMWPE composites have similar strengths, as do the CFRP-C and CFRP-U composites.

The tensile responses of the CFRP and UHMWPE composites in the ±45° orientations, again at an applied strain rate of 10<sup>-3</sup>s<sup>-1</sup>, are plotted in Figs. 3b through to 3d. The responses are now dominated by shearing of the matrix. Hence, the strength of the composites is significantly lower than in the 0° / 90° orientation and the composites also exhibit a higher ductility in the ±45° orientation. The HB26, HB50 and the CFRP-U composites have a relatively soft matrix and display considerable ductility (in excess of 20%) and we shall first consider these materials. After initial yield, the composites continue to deform by scissoring of the fibres oriented at ±45° with respect to the tensile axis. The resulting rotation of the fibres aligns them closer to tensile axis. This gives rise to a hardening response as seen in Figs. 3b and 3c with the composites finally failing by matrix cracking with no failure of the fibres. The CFRP-U and HB50 composites have a similar strength while the HB26 composite (which has a stronger matrix) exhibits a higher strength but lower ductility. In contrast, the CFRP-C composite (Fig. 3d) behaves in an elastic perfectly plastic manner, with a significantly higher strength of approximately 160 MPa and a relatively small ductility of 4%. The CRFP-C composite also fails by matrix cracking with no fibre failure.

---

<sup>3</sup> Hexcell Data Sheet: HexPly® 8552 UD Carbon Prepregs.

The inter-laminar shear response of the composites with the “soft” matrices (i.e. CFRP-U, HB26 and HB50) are plotted in Fig. 4 for two applied displacement rates of 1 mm/min and 500 mm/min. Clearly there is considerable rate dependence of the measured shear response. We proceed to document the deformation modes in these double-notch shear tests and, for the sake of brevity, focus on the HB26 composite. (The deformations observed in the HB26 composite are qualitatively similar to those in the HB50 and CFRP-U composites). Contours of the measured axial displacement  $u_1$  are shown in Fig. 5 at selected values of the applied displacement. These displacement contours on the surface of the double-notch specimen were obtained by digital image correlation in the test performed at the applied displacement rate of 1mm/min. Prior to peak load, the shear strain state is reasonably homogenous (i.e.  $\partial u_1 / \partial x_3$  is almost uniform). However, at peak stress and beyond, deformation strongly localises on two bands that emanate from the notches. Microscopic examination of each of these bands in post-tested specimens revealed that deformation was localised on a single inter-laminar plane and hence it is not meaningful to quote an applied strain or strain rate in these tests.

### 3. Static stretch-bend response of clamped beams

The four composites listed in Table 1 were first tested in a static stretch-bend configuration in order to provide a baseline reference for the dynamic tests reported subsequently. The beams were oriented such that one set of plies was aligned with the longitudinal axis of the beam. Beams of length 400 mm and width  $w = 35$  mm were cut from the manufactured plates (see Table 1 for the thickness  $h$  of the 4 plate types) and 5 holes of diameter  $d = 6$  mm drilled at each end of the beams in the pattern sketched in Fig. 6a. These beams were then bolted into the stretch-bend apparatus via M6 bolts and a 10 mm thick steel cover plate at each end as illustrated in Fig. 6b. The free-span of the beams was  $L = 200$  mm and the bolts were tightened to a torque of 9 Nm. The beams were loaded at mid-span via a cylindrical roller of diameter 19 mm and length 40 mm such that the beams were loaded uniformly across their width  $w$ . Loading was applied by displacing the roller at a rate 500 mm/min via a screw-driven test machine. The load cell of the test machine was used to measure the applied force  $F$  and the roller displacement  $\delta$  was measured via a laser extensometer.



The measured  $F$  versus  $\delta$  responses of the four composite beams is plotted in Fig. 7a. All the beams display a response where  $F$  increases approximately quadratically with  $\delta$ . The failure load increased in the order CFRP-C < CFRP-U < HB26 < HB50, indicating a strong sensitivity to matrix strength. Furthermore, the two UHMWPE beams have almost identical responses up to the instant of failure. All beams failed by fibre fracture at the supports as seen in the photographs in Fig. 8. The three beams with relatively soft matrices, i.e. the HB26, HB50 and CFRP-U beams failed by fibre fracture along the row of holes nearest to mid-span. Significant elongation of the bolt holes is observed for the CFRP-U beams while this is less obvious for the UHMWPE beams. On the other hand, the CFRP-C beam failed by fibre fracture adjacent to the clamped supports, i.e. not at the bolts.

Failure in all the tests occurred in the regime where the beams were deforming in a string-like mode with the tensile stresses (due to stretching) much greater than the bending stresses: the displacement of the roller exceeded the thickness  $h$  of the beams. The net-section stretching stress  $\sigma_t$  across a failed section is then given by a force balance as

$$\sigma_t = \frac{F}{2hw'\sin\theta} \quad (3.1)$$

where  $\tan\theta = 2\delta/L$ ,  $w'$  is the net-section width at the failure plane and  $d$  is the diameter of the bolt holes in the beams. Thus,  $w' = w - 2d$  for the UHMWPE and CFRP-U beams which failed at the bolt holes and  $w' = w$  for the CFRP-C beam; see Fig. 8. In the absence of stress concentrations associated with the clamping geometry, we would expect the beams to fail when  $\sigma_t = \sigma_f$ , where  $\sigma_f$  is the tensile failure strength of the  $0^\circ/90^\circ$  composites (Fig. 3a).

An apparent stress concentration can then be defined as  $K_\sigma = \sigma_f / \sigma_t^f$  where  $\sigma_t^f$  is the value of  $\sigma_t$  at the peak value of  $F$ . The values of  $K_\sigma$  for the four beams tested in this bolted configuration are listed in Table 2 and clearly show that significant stress concentrations exist. The stress concentrations are strongly dependent on the material with  $K_\sigma$  increasing in the order HB50 < HB26 < CFRP-U < CFRP-C. This indicates that  $K_\sigma$  not only depends on the shear strength of the matrix (HB50 has a lower value of  $K_\sigma$  than HB26) but is also dependent on the fibre type (CFRP-U has a higher value of  $K_\sigma$  than HB26 despite its lower

shear strength. The magnitude of the observed stress concentration  $K_\sigma$  is also strongly dependent on the clamping geometry. We proceed to investigate the effect of clamping geometry upon the stretch-bend response of the beams.

### 3.1 *Effect of clamping geometry*

For the sake of brevity we restrict attention to the UHMWPE beams. Since the beams failed at the bolts we designed a clamping arrangement that avoided bolting through the beams. This was achieved by wrapping the ends of the beams around mandrels as sketched in Fig. 9. These beams were not cut from pre-prepared plates as supplied by DSM Dyneema. Rather, the composites, of lay-up as given in Table 1, were laid-up from uncured plies which had been supplied by DSM Dyneema. The plies at the ends of the beam were wrapped around 5 aluminium mandrels as illustrated in Fig. 9a such that the 96 plies of the beams were evenly distributed between the 5 mandrels. Beams (with mandrels in situ) were hot pressed according to the standard recipe (20 MPa at 120° C for 15 mins). The mandrels of the cured beams were then slotted into a steel fixture as sketched in Fig. 9b and a 10 mm thick steel plate was bolted on top, see Fig. 9b. Four M6 bolts held this clamping plate in place by tightening them to a torque of 9 Nm. (Note that the bolts did not pass through the beams in this case.) The measured  $F$  versus  $\delta$  responses of the HB50 and HB26 beams are plotted in Fig. 7b. Two main differences are apparent compared to the bolted beams: (i) the peak forces and associated displacements are significantly higher for the wrapped beams than for the bolted beams and (ii) failure is not abrupt but rather more gradual with multiple load drops corresponding to a progressive failure of plies. In contrast, all plies fail simultaneously in the bolted beams. The gradual failure of the plies in the wrapped beams is seen in the photograph (Fig. 10a) of a HB50 beam taken at  $\delta = 65$  mm: some of the plies of the beam have failed at the corner of the topmost mandrel with the remainder of the plies intact. A sketch of the ply fracture modes at the wrapped ends as deduced from the photographs is included in Fig. 10c in order to clarify the fracture phenomena.

The increase in peak force with change in clamping arrangement suggests that we might have succeeded in reducing the stress concentration  $K_\sigma$  at the clamped ends by removing the bolt holes. The values of  $K_\sigma$  inferred from the peak force measurements are included in Table 2

( $w' = w$  in this case as there are no bolt holes through these beams). Surprisingly,  $K_\sigma$  has increased, i.e. the deduced stress concentration due to the bolted ends is less than the stress concentration that results from wrapping the beams around the mandrels. The increase in the peak force is due to the fact that the net section carrying the load in the wrapped beams has an area  $wh$  while in the bolted beams only an area  $(w - 2d)h$  carries tensile stress.

#### 4. Dynamic foam impact response

The use of foam projectiles as a means of providing well-characterised pressure versus time loading on a structure has recently been developed by Radford et al. [24] and has been subsequently employed to investigate the dynamic response of sandwich beams with lattice cores (Radford et al. [25]), and of sandwich plates with both metal foam cores (Radford et al. [26]) and lattice cores (McShane et al. [27]). Liu et al. [23] have shown that a metal foam projectile is adequate for representing the impact of beams by a sand particle column of similar momentum. Consequently, the metal foam projectile is a useful surrogate to investigate the response of a beam to landmine loading. We proceed to report the dynamic response of the bolted CFRP and UHMWPE beams (with lay-ups as listed in Table 1) and then investigate the effect of the clamping geometry upon the dynamic performance in an analogous manner to the static stretch-bend tests reported above.

##### 4.1 Dynamic test protocol

Alporas aluminium foam projectiles were used to provide impact loading of the laminate beams over a central circular patch, as shown in Fig. 11. Circular cylindrical projectiles of length  $\ell = 50$  mm and diameter  $D = 28.5$  mm were electro-discharge machined from Alporas foam blocks of density  $\rho_p = 200$  kg m<sup>-3</sup>. The projectiles were fired from a gas gun of bore diameter 28.6 mm and length 4.5 m, at a velocity  $v_0$  between 140 ms<sup>-1</sup> and 890 ms<sup>-1</sup>, providing a projectile momentum per unit area in the range  $I_o = \rho_p \ell v_0 = 1 - 10.6$  kNs m<sup>-2</sup>. High-speed photography was employed to observe the dynamic transverse deformation of the beams; a Phantom V12 camera was used to take images typically with an inter-frame time of 25.6  $\mu$ s and an exposure time of 0.3  $\mu$ s.

#### 4.2 *Dynamic response of bolted beams*

Montages of high speed images showing the deformation of the HB26, HB50, CFRP-U and CFRP-C beams are given in Figs. 12, 13, 14 and 15, respectively. In part (a) of these figures, a value of  $I_0$  is chosen where the beams remain intact while in part (b) images are shown for the value of  $I_0$  when fracture of the beams at the supports was first observed. The corresponding measured mid-span deflection  $\delta$  versus time  $t$  curves (where  $t=0$  corresponds to the instant that the foam projectile impacts the beams) are shown in Figs. 16a and 16b for the UHMWPE and CFRP beams respectively.

First, consider the UHMWPE beams. The high speed images in Figs. 12 and 13 show that plastic hinges emanate from the impact location and travel towards the supports in a similar manner to that observed for metallic beams [25]. However, there is a key difference: in metallic beams bending travelling hinges were generated by the impact process while inter-laminar shear is the dominant deformation mechanism within the hinges in both the HB50 and HB26 beams (the black vertical lines drawn on the UHMWPE beams remain vertical during deformation). We also note that negligible delamination is observed during the dynamic deformation of the beams and failure occurs by the entire beam being pulled out of the supports at one end. Photographs of the failed ends of the HB26 and HB50 beams are included in Figs. 17a and 17b, respectively. A comparison with the corresponding images of the failed ends in the quasi-static stretch-bends tests (Fig. 8) clearly show that the failure mechanisms are the same in the static and dynamic tests. Moreover, there is no discernable difference between the observed failure mode in the HB26 and HB50 beams. In fact, the HB50 and HB26 beams have nearly identical deflection versus time responses (Fig. 16a) with the only difference being that the HB50 beams fails at a higher value of  $I_0$ .

Next, consider the CFRP beams. The deformation mechanism of the CFRP-U beam at low values of  $I_0$  is similar to the UHMWPE beams: travelling shear hinges emanate from the impact site and propagate towards the supports. However, in contrast to the UHMWPE beams, extensive delamination occurs in the CFRP-U beams even at values of  $I_0$  where no ply failure is observed. Travelling hinges are not observed in the CFRP-C beams although significant delamination occurs in this case too. The high-speed images again show that both

beam types fail at the supports and photographs of the failed ends in Fig. 17 illustrate that the failure mechanism is again similar to the static tests; i.e. the CFRP-U beams pull-out and fail by fibre fracture across the section through the bolt holes while the CFRP-C beams have a significantly more brittle failure mode with fracture occurring at the edge of the clamped supports. As for the UHMWPE beams, the CFRP-C and CFRP-U beams have similar mid-span deflection versus time responses (Fig. 16b) for all values of  $I_0$  less than that required to trigger failure in the CFRP-C beams. Moreover, the failure impulse for the CFRP-U beams is higher than that for the CFRP-C beams. Thus, in both the UHMWPE and CFRP beams there is a clear trend that decreasing the shear strength of the beams increases the failure impulse.

The maximum mid-span deflections  $\delta_{\max}$  versus projectile impulse  $I_0$  are plotted in Fig. 18a for the four beam types investigated here and best-fit straight lines are put through the measured data. The failure of the beams is indicated by an upward pointing arrow denoting that the maximum deflections of the beams become unbounded for values of  $I_0$  exceeding that critical impulse. The deflections  $\delta_{\max}$  are typically higher for the CFRP beams than for the UHMWPE beams for the same value of  $I_0$  while the impulses  $I_f$  at which failure occurs are higher for the UHMWPE beams. We again emphasise that for a given fibre type,  $I_f$  increases with decreasing matrix shear strength; compare the  $I_f$  values of CFRP-C versus CFRP-U and HB26 versus HB50 in Fig. 18a.

The large deflections observed for the UHMWPE and CFRP-U beams are anticipated to be a result of both tensile straining and consequent elongation of the beams as well as the pull-out of the beams from their supports. To quantify the relative importance of these two contributions to the deflections of the beams we define the pull-out  $L_p$  as the horizontal displacement of a boundary marker at the clamped supports as sketched in Fig. 19a. The deflection  $\delta_p$  solely due to pull-out is then given as

$$\delta_p = \sqrt{L_p(L_p + L)} \quad (4.1)$$

The temporal evolution of  $L_p$  for the HB26 beams as measured from high-speed photographs is plotted in [Fig. 19b](#) for two values of the impulse  $I_0$ . In both cases,  $L_p$  first increases with time  $t$  and then reaches a steady-state. From Eq. (4.1) we estimate the deflections  $\delta_p$  due to the pull-out at steady-state as  $\delta_p \approx 12$  mm and 16 mm for the  $I_0 = 1.54$  kPa s and 3.67 kPa s cases respectively. These deflections are approximately equal to the maximum observed deflections (see [Fig. 18a](#)) which suggests that the deflections are mainly a result of pull-out with negligible tensile straining of the beams<sup>4</sup>. The pull-out reaches its maximum value well before the travelling hinges reach the supports. For example for the  $I_0 = 3.67$  kPa s case, hinges reach the supports between 179  $\mu$ s and 203  $\mu$ s after impact ([Fig. 12a](#)) while pull-out is complete by about 150  $\mu$ s ([Fig. 19b](#)). This is because pull-out is initiated by the high speed longitudinal elastic wave that travels along the fibre and reaches the supports very soon after the impact event while the travelling hinges are due to shear deformations and hence have a much lower wave speed in this highly anisotropic material.

The same conclusions were drawn from a similar analysis on the HB50 and CFRP-U beams. However, there was negligible pull-out for the CFRP-C beams which implied that the deflections in those beams was due to tensile straining of the beams as discussed by [Russell et al. \[29\]](#).

#### 4.3 *Dynamic response of the wrapped UHMWPE beams*

The above results demonstrate that the clamping geometry significantly affects the dynamic response of the beams. Following the same strategy as for the quasi-static stretch-bend tests we conducted additional impact tests on wrapped HB50 and HB26 beams. The maximum deflection  $\delta_{\max}$  is plotted in [Fig. 18b](#) as a function of  $I_0$ , along with the results from [Fig. 18a](#) for the bolted HB26 and HB50 beams. Two main differences are observed: (i) the deflections of the wrapped beams are higher than those of the bolted beams for all values of  $I_0$  prior to failure and (ii) the impulses  $I_f$  at which the beams fail are also significantly higher compared to the corresponding bolted beams. Recall that for the bolted beams, the failure impulse  $I_f$

---

<sup>4</sup> Measurements of the transient lengths of the beams from the high-speed images also led to the conclusion that the beams undergo negligible overall tensile strains.

for the HB50 beams is about 20% higher than that for the HB26 beams. This results also holds for the wrapped beams; we note in passing that we were unable to achieve complete failure of the wrapped HB50 at the maximum projectile velocity achievable ( $v_0 = 890 \text{ ms}^{-1}$ ) with the single stage gas gun used in this investigation.

Similar to the quasi-static stretch-bend tests, failure of the wrapped beams occurs at the corner of the top mandrel. In contrast to the sudden failure of the bolted beams, failure of the wrapped beams is gradual with progressive ply breaking at  $I_0 < I_f$  (see the photograph in [Fig. 10b](#) showing the partial failure of the HB50 beam for  $I_0 = 8.3 \text{ kPa s}$ ) with all plies breaking at the corner of the top mandrel for impulses greater than  $I_f$ . The impulse at which ply failure is first observed is included in [Fig. 18b](#):  $I_f$  is approximately 10% larger than the impulse for first ply failure in the HB26 beams.

## 5. Comparison between dynamic and quasi-static rankings of the beams

The above results from the quasi-static stretch-bend tests and from the impact tests suggest that the initial deformation mode under dynamic loading is markedly different from the static case and comprises travelling hinges. However, once the hinges reach the supports, the deformation modes in the dynamic and static cases are similar and resemble that of a plastic stretching string. It is thus not surprising that the failure modes in both the static and dynamic cases are similar and involve the tensile fracture of the fibres at the supports. Thus, we examine whether the failure loads in the static stretch-bend tests is indicative of the performance in impact tests.

First consider the bolted beams. Recall that failure of these beams is a sudden event with all plies failing together in both the static and dynamic tests. The peak load  $F_{\max}$  in the static tests and the impulse  $I_f$  corresponding to this failure event are plotted in the bar chart in [Fig. 20](#). The ranking of the beams in the static stretch-bend tests agrees with the ranking in the dynamic tests for all four beam types investigated here. Next, consider the wrapped UHMWPE beams and recall that failure was a gradual process with successive plies failing

above a critical impulse until all plies had failed at the failure impulse  $I_f$ . Again it is clear that the static ranking in terms of  $F_{\max}$  corresponds to the ranking  $I_f$ . We conclude that static-stretch-bend tests provide an excellent indication of the failure mechanism of the beams under soft impact loading. Moreover, these static tests can be used to rank the dynamic performances of these beams in terms of their failure impulse.

## 6. Concluding remarks

The quasi-static and dynamic impact responses of CFRP and UHMWPE laminate beams with clamped ends were investigated for beams of aerial mass about  $6 \text{ kg m}^{-2}$ . Two variants of each of these composites were investigated in order to quantify the effect of matrix shear strength: (i) CFRP laminates with a cured and uncured matrix and (ii) the HB26 and HB50 UHMWPE laminates manufactured by DSM Dyneema which have a the same fibre type but a high and low shear strength, respectively. The effect of clamping geometry was investigated by considering beams bolted into their clamped supports and beams wrapped around mandrels at the clamped ends.

In the quasi-static stretch-bend tests, all beams failed by tensile fracture of the fibres at the clamped supports. The UHMWPE beams had a larger load carrying capacity than the CFRP beams, and for both the CFRP and UHMWPE beams, a reduction in matrix shear strength resulted in an increase in failure load. Tensile fracture of the bolted beams occurred at the bolt holes and we deduced the effective stress concentration  $K_\sigma$  at the supports from the measured failure load of the beams. This indicated that a reduction in shear strength of the matrix reduces  $K_\sigma$  at the supports and thereby increases the load carrying capacity of the beams. Surprisingly,  $K_\sigma$  for the beams with wrapped ends is approximately equal to that for the beams with bolt holes suggesting that a significant stress concentration is also generated at the corner of the mandrels around which the plies are wrapped. However, the beams with wrapped ends have a larger load carrying capacity compared to the bolted beams as the absence of the bolt holes means that they have a larger net-sectional area.



The deformation mode of the beams under soft projectile impact is markedly different from the quasi-static stretch-bend tests. Travelling shear hinges emanate from the impact location and propagate towards the supports. Once these hinges reach the supports, the modes under dynamic and static loading are similar and resemble that of a plastic stretching string. Failure occurs in this string-like mode due to tensile fracture of the fibres at the supports, in similar manner to the static case.

The ranking of the beams under dynamic loading is identical to that under static loading, with the wrapped beams sustaining higher dynamic impulses compared to the bolted beams. Also, the beams with a lower strength matrix can sustain a higher impulse to failure. In summary, the UHMWPE beams show significant promise for application to mitigation of blast loading. Moreover, the static stretch-bend tests can be used to rank the relative performances of these beams for soft impact or blast loading applications. However, while we have experimentally shown that reducing the shear strength typically enhances the load carrying capacity of the beams, the precise mechanisms leading to this remain to be elucidated. This remains a topic for future numerical/theoretical studies.

### **Acknowledgments**

This research was supported by the Office of Naval Research (ONR NICOP grant number N00014-09-1-0573) as part of a Multidisciplinary University Research Initiative on “Cellular materials concepts for force protection”, Prime Award No. N00014-07-1-0764 is gratefully acknowledged. The program manager was Dr David Shifler. The authors also wish to thank DSM Dyneema for supplying the HB26 and HB50 laminate plates, and technical discussion facilitating the experimental programme. Dyneema<sup>®</sup> is a trademark of DSM.

## References

- [1] Hearle JWS. High-performance fibres. Woodhead Publishing; 2001
- [2] Cunniff PM. Dimensionless parameters for optimization of textile-based body armor systems, in: Reinecke WG (Ed.). Proceedings of the 18th International Symposium on Ballistics, San Antonio, TX. Lancaster: Technomic; 1999
- [3] Phoenix SL, Porwal PK. A new membrane model for the ballistic impact response and V50 performance of multi-ply fibrous systems. *Int J Solids Struct* 2003;40:6723-65
- [4] Wilding MA, Ward IM. Tensile creep and recovery in ultra-high modulus linear polyethylenes. *Polym* 1978;19:969-76
- [5] Wilding MA, Ward IM. Creep and recovery of ultra high modulus polyethylene. *Polym* 1981;22:870-6
- [6] Wilding MA, Ward IM. Creep and stress-relaxation in ultra-high modulus linear polyethylene. *J Mater Sci* 1984;19:629-36
- [7] Jacobs M, Heijnen N, Bastiaansen C, Lemstra PJ. A novel, efficient route for the crosslinking and creep improvement of high modulus and high strength polyethylene fibres. *Macromol Mater Eng* 2000;283:120-5
- [8] Govaert LE, Lemstra PJ. Deformation behavior of oriented UHMW-PE fibers. *Colloid Polym Sci* 1992;270:455-64
- [9] Peijs A, Catsman P, Govaert LE, Lemstra PJ. Hybrid composites based on polyethylene and carbon fibres Part 2: influence of composition and adhesion level of polyethylene fibres on mechanical properties. *Composites* 1990;21:513-21
- [10] Govaert LE, Bastiaansen C, Leblans P. Stress-strain analysis of oriented polyethylene. *Polym* 1993;34:534-40
- [11] Kromm F, Lorriot T, Coutand B, Harry R, Quenisset JM. Tensile and creep properties of ultra high molecular weight PE fibres. *Polym Test* 2003;22:463-70
- [12] Dessain B, Moulart O, Keunings R, Bunsell AR. Solid phase change controlling the tensile and creep behaviour of gel-spun high-modulus polyethylene fibres. *J Mater Sci* 1992;27:4515
- [13] Huang W, Wang Y, Xia Y. Statistical dynamic tensile strength of UHMWPE-fibers. *Polym* 2004;45:3729-34
- [14] Koh ACP, Shim VPW, Tan VBC. Dynamic behaviour of UHMWPE yarns and addressing impedance mismatch effects of specimen clamps. *Int J Impact Eng* 2010;37:324-32

- [15] Benloulou IC, Rodriguez J, Martinez MA, Galvez VS. Dynamic tensile testing of aramid and polyethylene fiber composites. *Int J Impact Eng* 1997;19:135-46
- [16] Koh C, Shim V, Tan V, Tan B. Response of a high-strength flexible laminate to dynamic tension. *Int J Impact Eng* 2008;35:559-68
- [17] Frissen RJT. Modelling the Ballistic Impact Behaviour of Polyethylene-Fibre-Reinforced Composites. Eindhoven: University of Technology; 1996
- [18] Russell BP, Karthikeyan K, Deshpande VS, Fleck NA. The high strain rate response of Ultra High Molecular-weight Polyethylene: from fibre to laminate. Submitted to *Int J Impact Eng* 2012
- [19] Grujicic M, Glomski PS, He T, Arakere G, Bell WC, Cheeseman BA. Material Modeling and Ballistic-Resistance Analysis of Armor-Grade Composites Reinforced with High-Performance Fibers. *J Mater Eng Perform* 2009;18:1162-82
- [20] Grujicic M, Arakere G, He T, Bell WC, Glomski PS, Cheeseman BA. Multi-scale ballistic material modeling of cross-plyed compliant composites. *Composites Part B* 2009;40:468–82
- [21] Iannucci L, Pope D. High velocity impact and armour design. *Express Polym Lett* 2011;5:262-72
- [22] Park S, Uth T, Fleck NA, Wadley HNG, Deshpande VS. Sand column impact with a rigid target. Submitted to *Int J Impact Eng* 2012
- [23] Liu T, Fleck NA, Deshpande VS, Wadley HNG. The impact of sand slugs against beams and plates: coupled discrete/continuum calculations. *Int J Impact Eng In Press*
- [24] Radford DD, Deshpande VS, Fleck NA. The use of metal foam projectiles to simulate shock loading on a structure. *Int J Impact Eng* 2005;31:1152-71
- [25] Radford DD, Fleck NA, Deshpande VS. The response of clamped sandwich beams subjected to shock loading. *Int J Impact Eng* 2006;32:968-87
- [26] Radford DD, McShane GJ, Deshpande VS, Fleck NA. The response of clamped sandwich plates with metallic foam cores to simulated blast loading. *Int J Solids Struct* 2006;43:2243-59
- [27] McShane GJ, Radford DD, Deshpande VS, Fleck NA. The response of clamped sandwich plates with lattice cores subjected to shock loading. *Eur J Mech—A/Solids* 2006;25:215-29
- [28] Rathbun HJ, Radford DD, Xue Z, He MY, Yang J, Deshpande VS, Fleck NA, Hutchinson JW, Zok FW, Evans AG. Performance of metallic honeycomb-core sandwich beams under shock loading. *Int J Solids Struct* 2006;43:1746-63

- [29] Russell BP, Liu T, Fleck NA, Deshpande VS. The soft impact of composite sandwich beams with a square-honeycomb core. *Int J Impact Eng* 2012;48:65-81
- [30] Smith P, Lemstra PJ, Kalb B, Pennings AJ. Ultrahigh-Strength Polyethylene Filaments by Solution Spinning and Hot Drawing. *Polym Bull* 1979;1:733-6
- [31] Smith P, Lemstra P. Ultra-high-strength polyethylene filaments by solution spinning/drawing. *J Mater Sci* 1980;15:505-14
- [32] Daniel IM, Ishai O. *Engineering Mechanics of Composite Materials*, Oxford University Press, New York, Second Ed., 2005.
- [33] Liu G, Thouless MD, Deshpande VS, Fleck NA. Collapse mechanisms of a UHMWPE laminated beam, Submitted to *Int J Solids Struct* 2012.

## Tables

Table 1: Constituent and construction details for the four laminate material systems.

Laminate	Fibre	Matrix	Lay-up & thickness $h$	Fibre volume fraction $V_f$
HB26	SK76	Polyetherdiol-aliphatic	$[0^\circ/90^\circ]_{48}$	0.83
	$\text{\O}17 \mu\text{m}$	diisocyanate polyurethane	$h = 6.0 \text{ mm}$	
HB50	SK76	Styrene-isoprene-styrene	$[0^\circ/90^\circ]_{54}$	0.82
	$\text{\O}16 \mu\text{m}$	triblock copolymer	$h = 6.0 \text{ mm}$	
CFRP-C	IM7	Epoxy fiberite 934	$[(0^\circ/90^\circ)_7 0^\circ]$	0.55
	$\text{\O} 5.0 \mu\text{m}$	(cured – 2 hrs@120°C, 6 Bar)	$h = 3.8 \text{ mm}$	
CFRP-U	IM7	Epoxy fiberite 934	$[(0^\circ/90^\circ)_7 0^\circ]$	0.55
	$\text{\O} 5.0 \mu\text{m}$	(uncured)	$h = 4.0 \text{ mm}$	

Table 2: Values of the effective stress concentration factor  $K_\sigma$  as inferred from the static stretch-bend tests on the 4 types of bolted composite beams and the wrapped HB50 and HB26 beams.

Clamping condition	Beam designation	Stress concentration $K_\sigma$
Bolted	CFRP-C	6.39
	CFRP-U	2.49
	HB26	2.38
	HB50	1.96
Wrapped	HB26	4.07
	HB50	2.39

## Figure Captions

Fig. 1: Materials typically used for ballistic protection applications plotted in longitudinal wave speed versus specific energy absorption space. Contours of constant Cunniff velocity  $c^*$  are included to indicate the best ballistic materials.

Fig. 2: Sketches of the specimens used to measure (a) the tensile responses of the laminates in the  $0^\circ/90^\circ$  and  $\pm 45^\circ$  orientations and (b) the inter-laminar shear response using a double-notch shear specimen. All dimensions are in mm.

Fig. 3: The measured tensile stress versus strain response of (a)  $0^\circ/90^\circ$  laminates made from the CFRP and UHMWPE laminates. The tensile response of  $\pm 45^\circ$  laminates are plotted for (b) HB26, (c) HB50 and CFRP-U and (d) CFRP-C composites. All responses are for an applied strain rate of  $10^{-3} \text{ s}^{-1}$ .

Fig. 4: The measured inter-laminar shear stress  $\tau_{31}$  versus applied shear displacement  $\Delta$  responses of the (a) the HB26, (b) HB50 and (c) CFRP-U laminates at applied displacement rates of 1 mm/min and 500 mm/min. The tests were performed using double-notch shear specimens, as sketched in Fig. 2b.

Fig. 5: The distribution of axial displacement  $u_1$  in the HB26 double-notch shear specimen at selected values of displacement  $\Delta$ . The distributions are reported for the test performed at an applied displacement rate of 1 mm/min using a DIC technique.

Fig. 6: (a) Sketch showing the leading dimensions of the bolted clamped beams and (b) a sketch of the set-up used to measure the static stretch-bend responses of these beams. All dimensions are in mm.

Fig. 7: The measured applied load versus displacement response in the quasi-static stretch-bend tests performed on the (a) bolted and (b) wrapped beams.

Fig. 8: Photographs of the failed clamped ends of the bolted beams in the quasi-static stretch-bend tests. (a) HB26, (b) HB50, (c) CFRP-C and (d) CFRP-U.

Fig. 9: (a) Sketch of the plies wrapped around the end mandrels for the wrapped HB50 and HB26 beams and (b) the setup used to clamp the wrapped ends.

Fig. 10: Photograph of the clamped end of the wrapped HB50 beams showing failure of some of the plies. Failure under (a) quasi-static stretch-bend loading after an applied displacement of  $\delta = 65$  mm and (b) dynamic loading with projectile impulse  $I_0 = 8.3$  kPa s. (c) A sketch of the mode of ply fracture at the wrapped ends.

Fig. 11: Sketch of the setup used to impact the clamped beams by a metal foam projectile. All dimensions are in mm.

Fig. 12: Time sequence of high-speed images of the bolted HB26 beams subjected to two levels of impulse (a)  $I_0 = 3.67$  kPa s, for which ply fracture was not observed and (b)  $I_0 = 4.48$  kPa s, for which the beams fail and pull out from the supports. Time  $t$ , as measured after the instant of impact, is recoded on each image.

Fig. 13: Time sequence of high-speed images of the bolted HB50 beams subjected to two levels of impulse (a)  $I_0 = 3.67$  kPa s at which ply fracture was not observed and (b)  $I_0 = 5.02$  kPa s at which the beams fail and completely pull-out of the supports. Time  $t$ , as measured after the instant of impact, is recoded on each image.

Fig. 14: Time sequence of high-speed images of the bolted CFRP-U beams subjected to two levels of impulse (a)  $I_0 = 4.02$  kPa s at which ply fracture was not observed and (b)  $I_0 = 6.83$  kPa s at which the beams fail and completely pull-out of the supports. Time  $t$ , as measured after the instant of impact, is recoded on each image.

Fig. 15: Time sequence of high-speed images of the bolted CFRP-C beams subjected to two levels of impulse (a)  $I_0 = 1.60$  kPa s at which no damage was observed and (b)  $I_0 = 2.90$  kPa s at which the beams fracture across the full section, at the supports. Time  $t$ , as measured after the instant of impact, is recoded on each image.

Fig. 16: Measured mid-span deflection  $\delta$  versus time  $t$  of (a) UHMWPE and (b) CFRP bolted beams. Time  $t = 0$  corresponds to the instant of impact.

Fig. 17: Photographs of the failed ends of the bolted beams subject to the metal foam impact with impulses  $I_f$ . (a) HB26, (b) HB50, (c) CFRP-C and (d) CFRP-U.

Fig. 18: The measured maximum deflections  $\delta_{\max}$  as a function of the projectile impulse  $I_0$  for the (a) four types of bolted beams and (b) the wrapped HB26 and HB50 beams. The deflections of the bolted HB26 and HB50 beams are included in (b).

Fig. 19: (a) Sketch illustrating the measurement of pull-out using a marker at the clamped supports and (b) the measured pull-out  $L_p$  versus time  $t$  for the bolted HB26 beams subject to two selected values of the projectile impulse  $I_0$ . Time  $t = 0$  corresponds to the instant of impact.

Fig. 20: A bar-chart illustrating the correspondence between the rankings of the beams in terms of the maximum force  $F_{\max}$  in the quasi-static stretch-bend tests and the failure impulses  $I_f$  in the dynamic soft impact tests, for both the bolted and wrapped clamped beams.



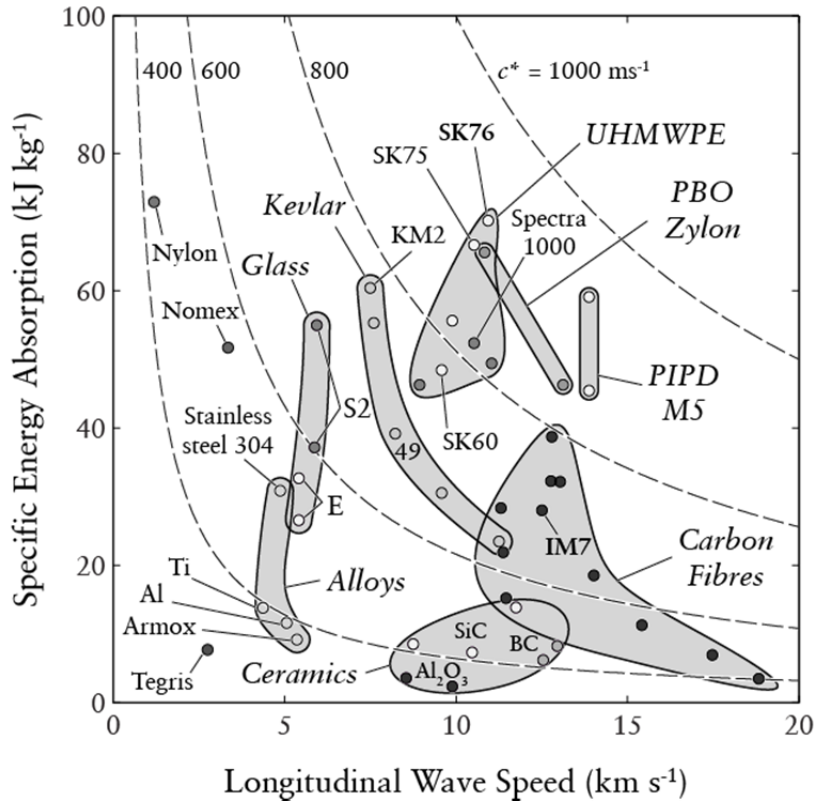


Fig. 1: Materials typically used for ballistic protection applications plotted in longitudinal wave speed versus specific energy absorption space. Contours of constant Cunniff velocity  $c^*$  are included to indicate the best ballistic materials.

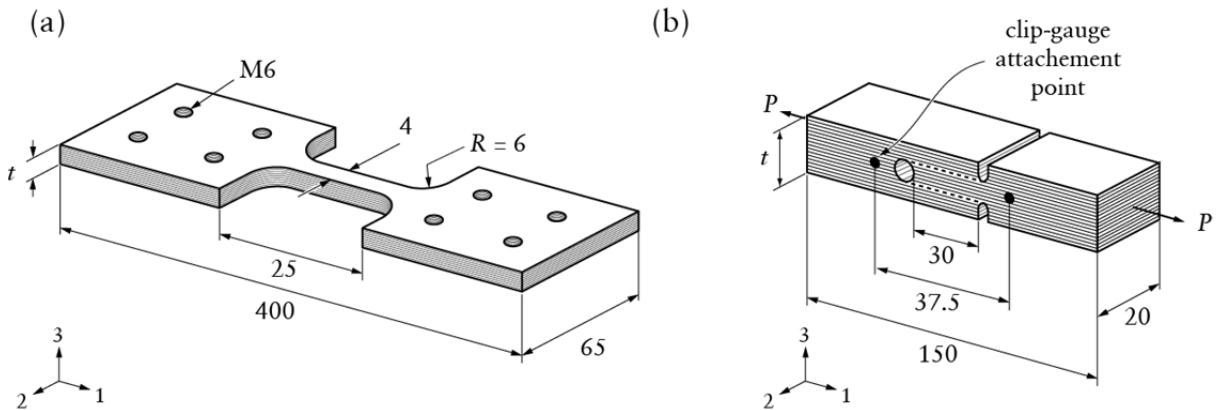


Fig. 2: Sketches of the specimens used to measure (a) the tensile responses of the laminates in the  $0^\circ/90^\circ$  and  $\pm 45^\circ$  orientations and (b) the inter-laminar shear response using a double-notch shear specimen. All dimensions are in mm.

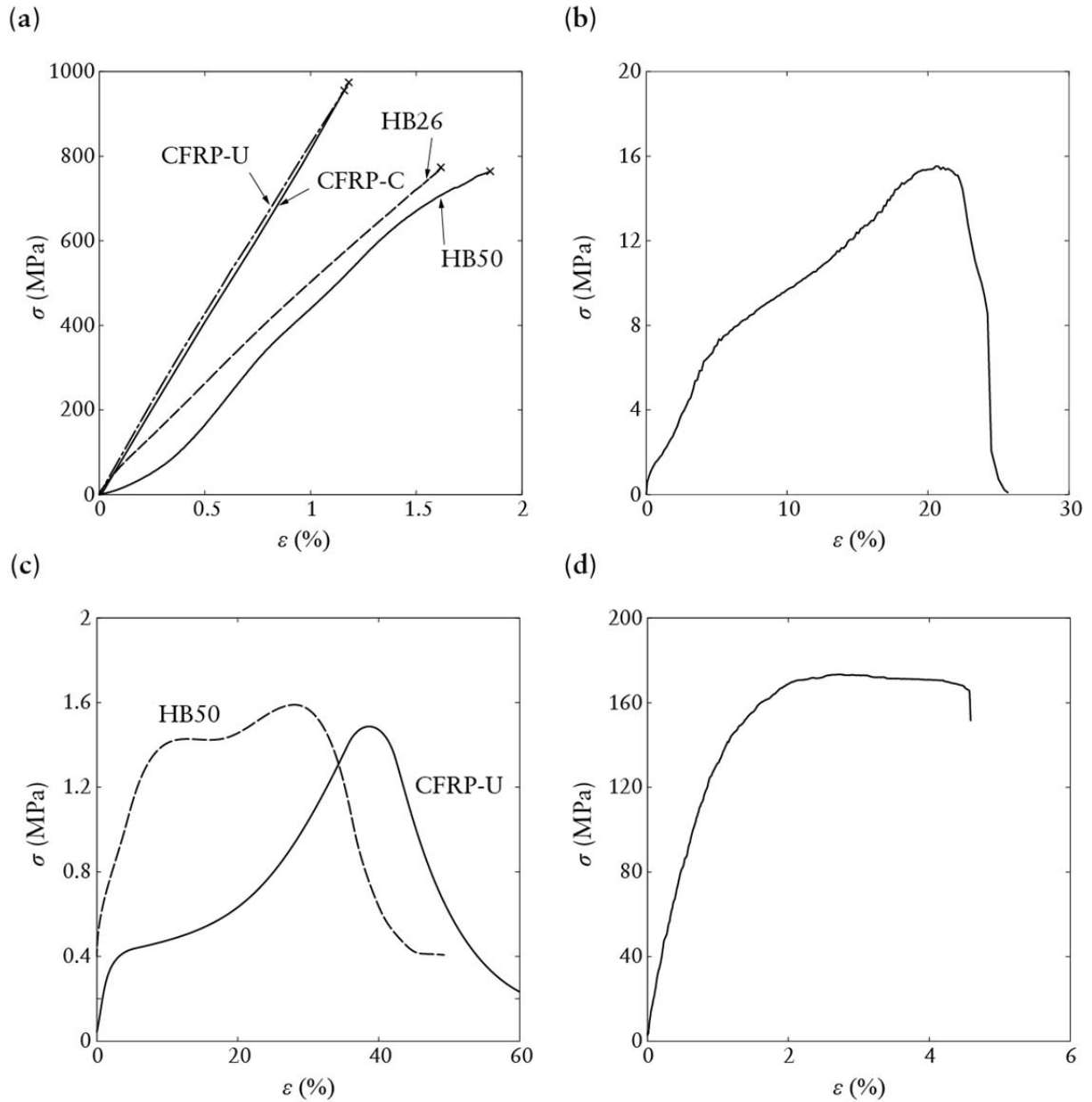


Fig. 3: The measured tensile stress versus strain response of (a)  $0^\circ/90^\circ$  laminates made from the CFRP and UHMWPE laminates. The tensile response of  $\pm 45^\circ$  laminates are plotted for (b) HB26, (c) HB50 and CFRP-U and (d) CFRP-C composites. All responses are for an applied strain rate of  $10^{-3} \text{ s}^{-1}$ .

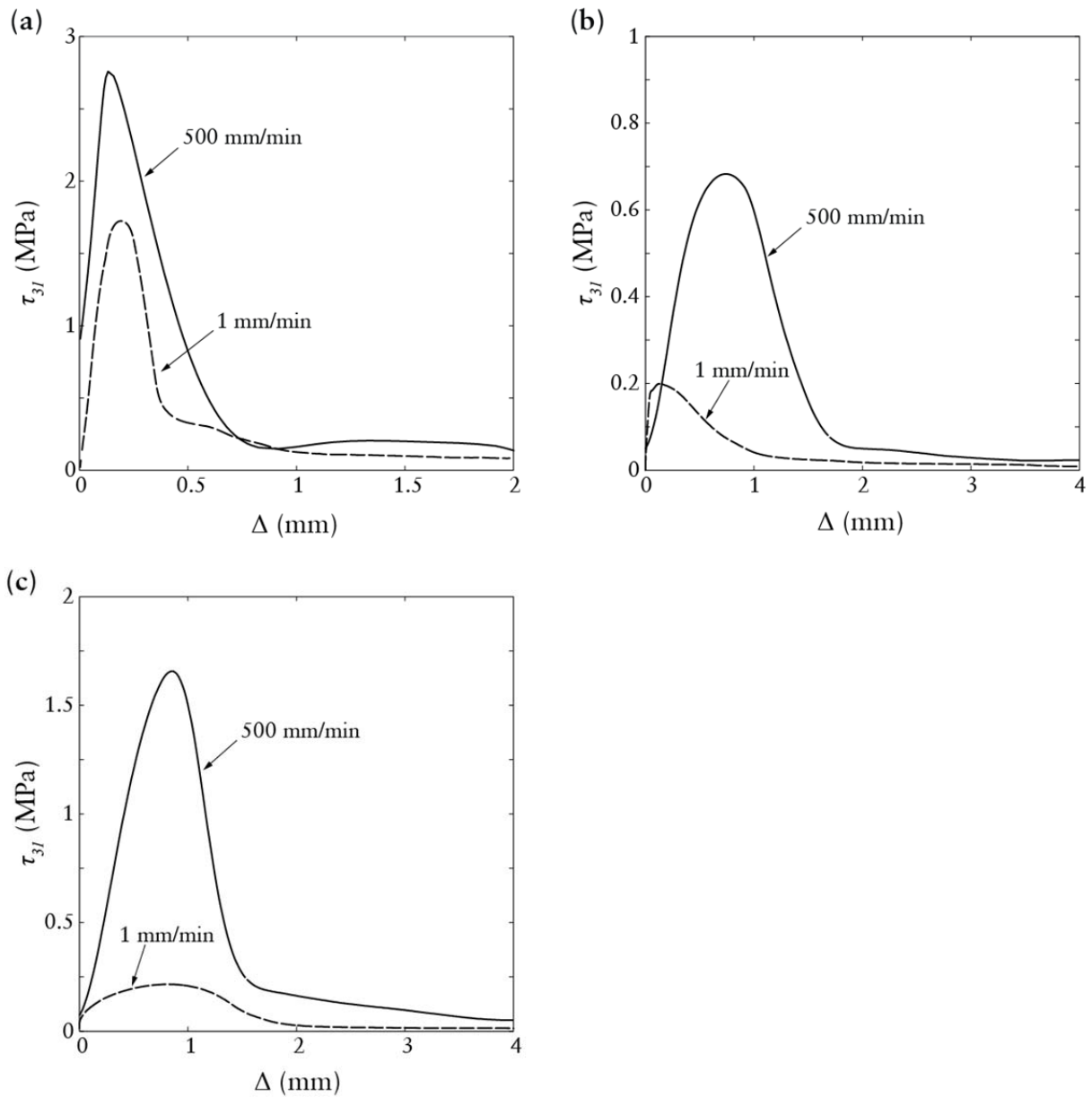


Fig. 4: The measured inter-laminar shear stress  $\tau_{31}$  versus applied shear displacement  $\Delta$  responses of the (a) the HB26, (b) HB50 and (c) CFRP-U laminates at applied displacement rates of 1 mm/min and 500 mm/min. The tests were performed using double-notch shear specimens, as sketched in Fig. 2b.

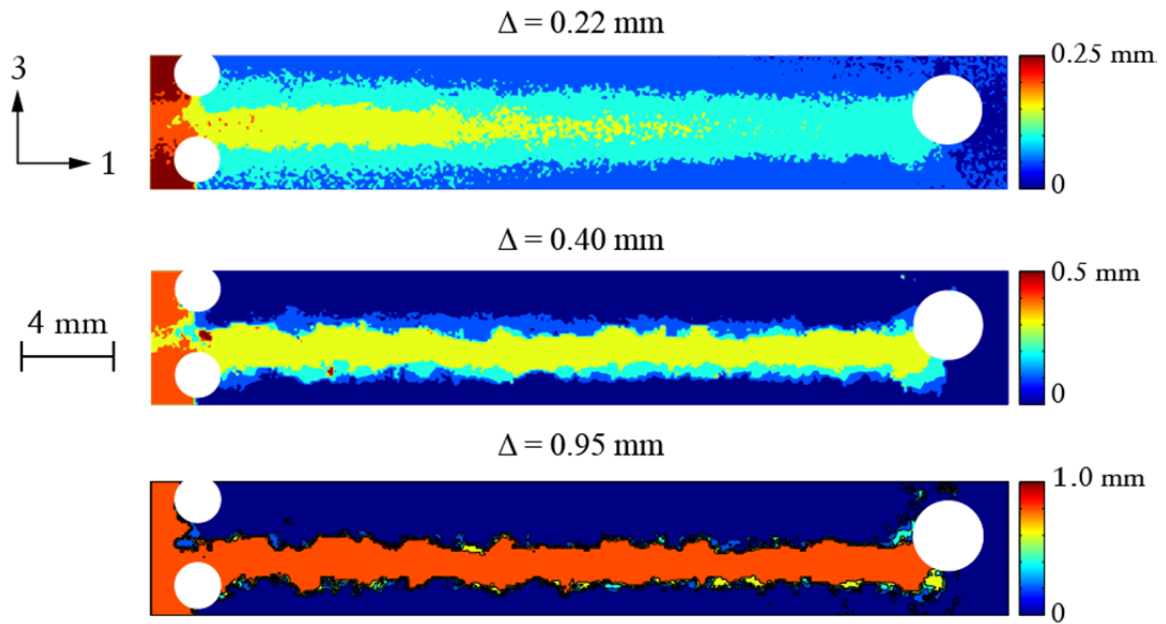


Fig. 5: The distribution of axial displacement  $u_1$  in the HB26 double-notch shear specimen at selected values of displacement  $\Delta$ . The distributions are reported for the test performed at an applied displacement rate of 1 mm/min using a DIC technique.

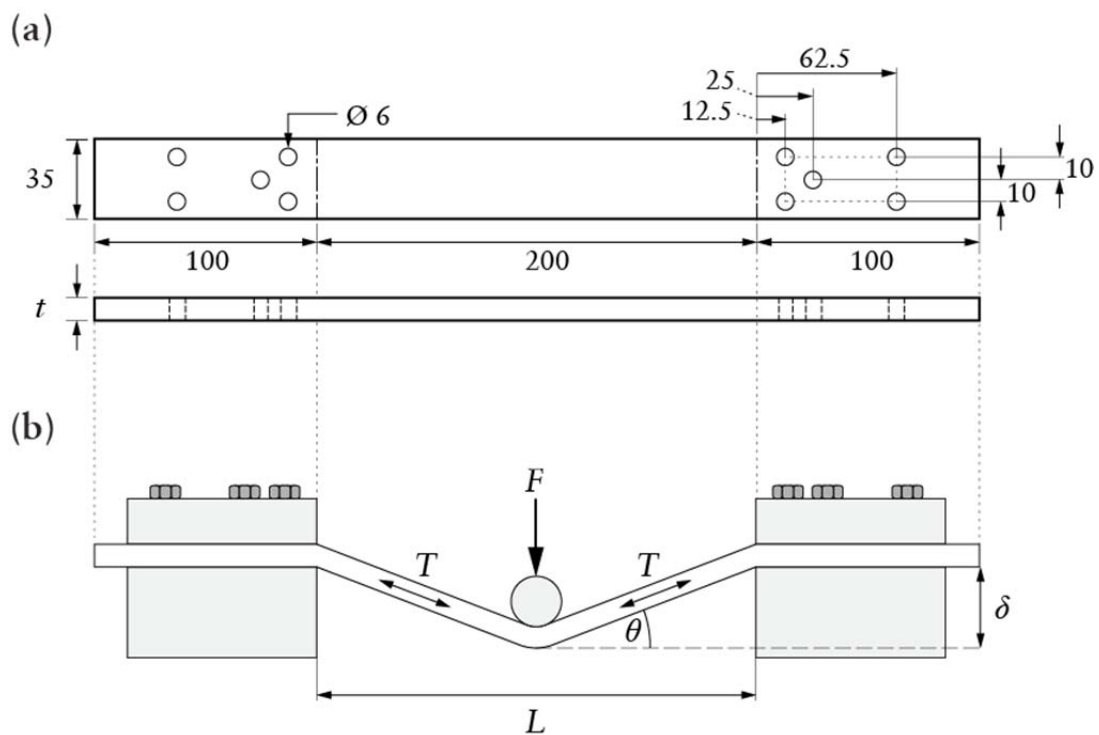


Fig. 6: (a) Sketch showing the leading dimensions of the bolted clamped beams and (b) a sketch of the set-up used to measure the static stretch-bend responses of these beams. All dimensions are in mm.

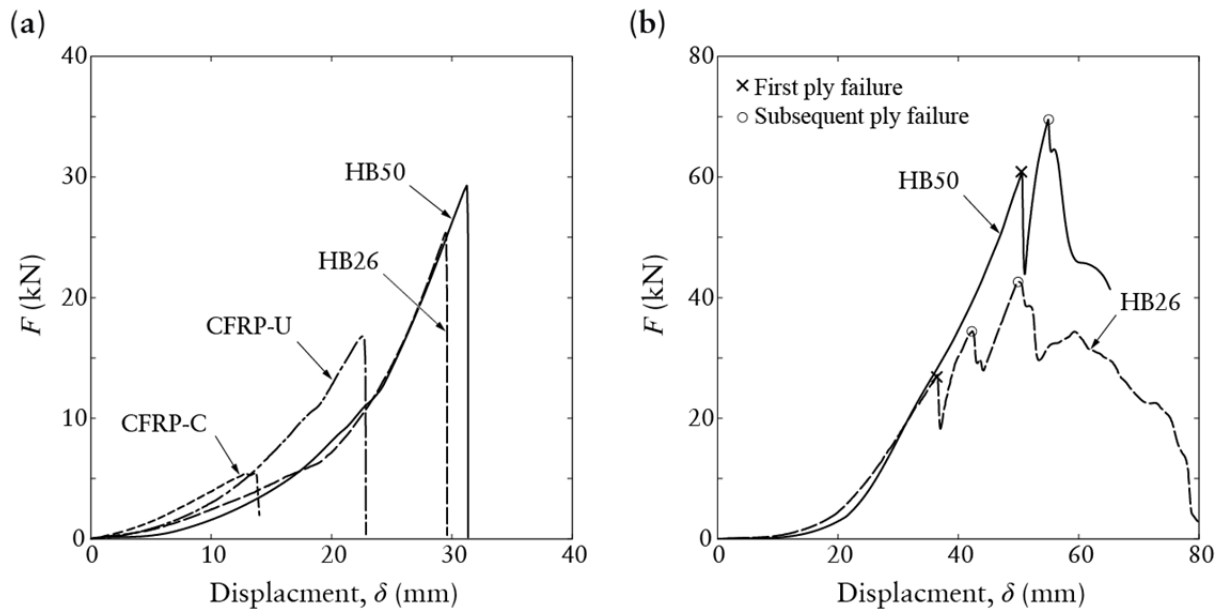


Fig. 7: The measured applied load versus displacement response in the quasi-static stretch-bend tests performed on the (a) bolted and (b) wrapped beams.

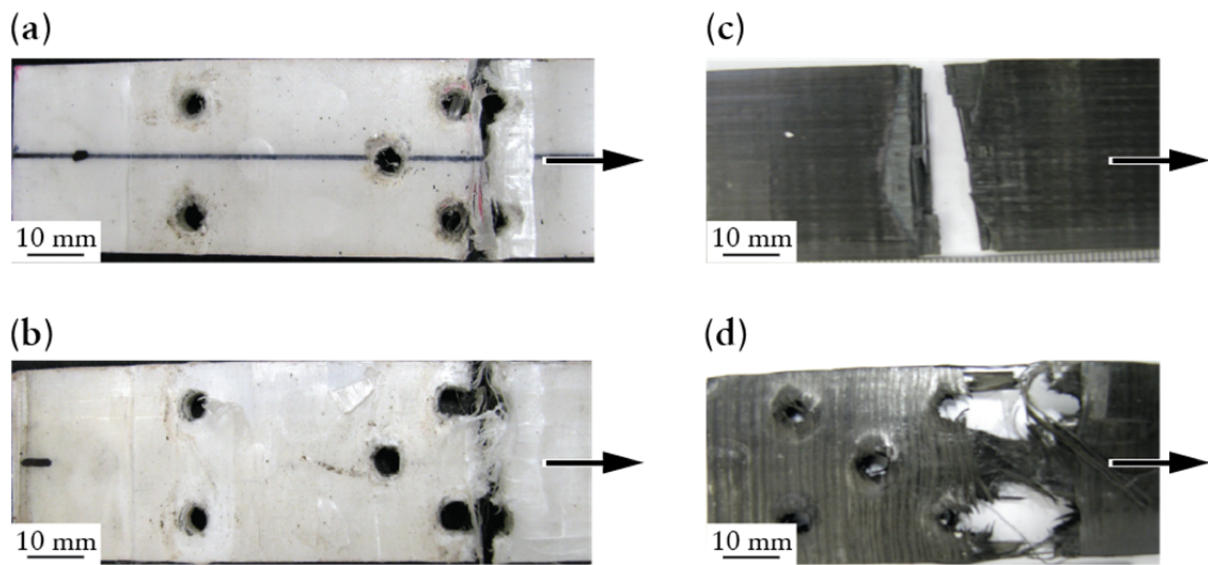


Fig. 8: Photographs of the failed clamped ends of the bolted beams in the quasi-static stretch-bend tests. (a) HB26, (b) HB50, (c) CFRP-C and (d) CFRP-U.

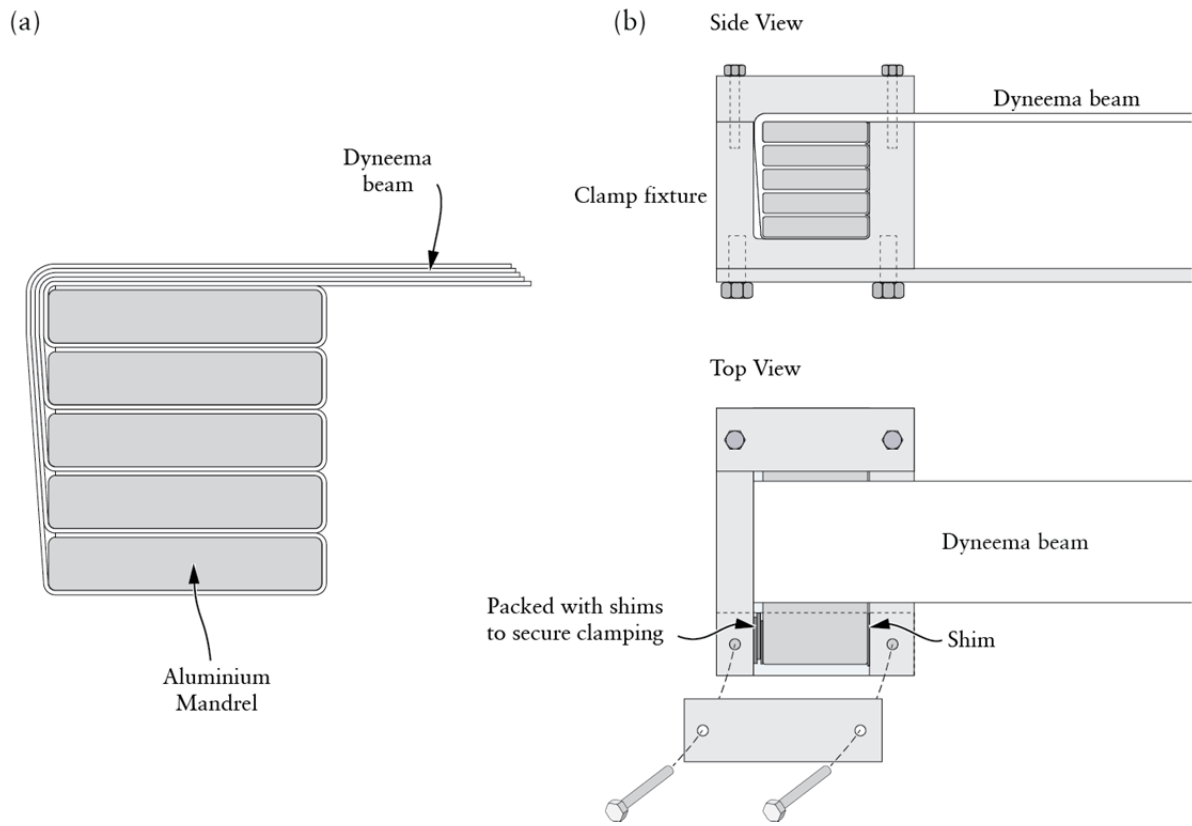


Fig. 9: (a) Sketch of the plies wrapped around the end mandrels for the wrapped HB50 and HB26 beams and (b) the setup used to clamp the wrapped ends.

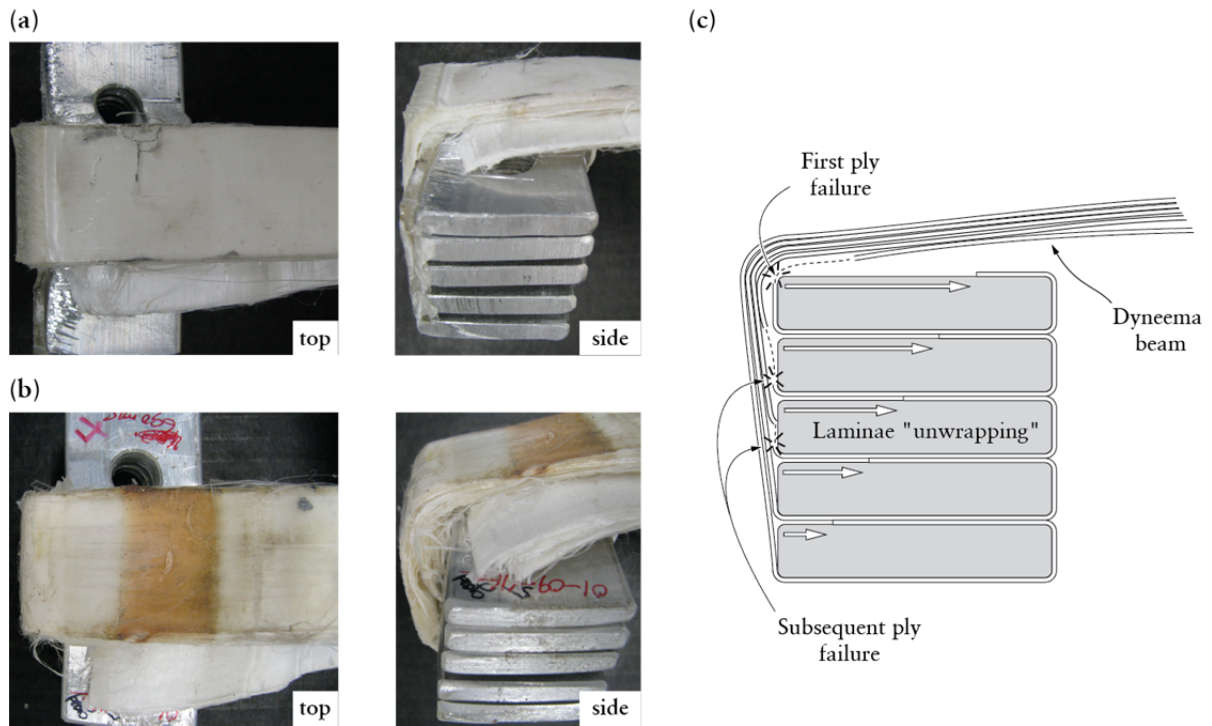


Fig. 10: Photograph of the clamped end of the wrapped HB50 beams showing failure of some of the plies. Failure under (a) quasi-static stretch-bend loading after an applied displacement of  $\delta = 65$  mm and (b) dynamic loading with projectile impulse  $I_0 = 8.3$  kPa s. (c) A sketch of the mode of ply fracture at the wrapped ends.

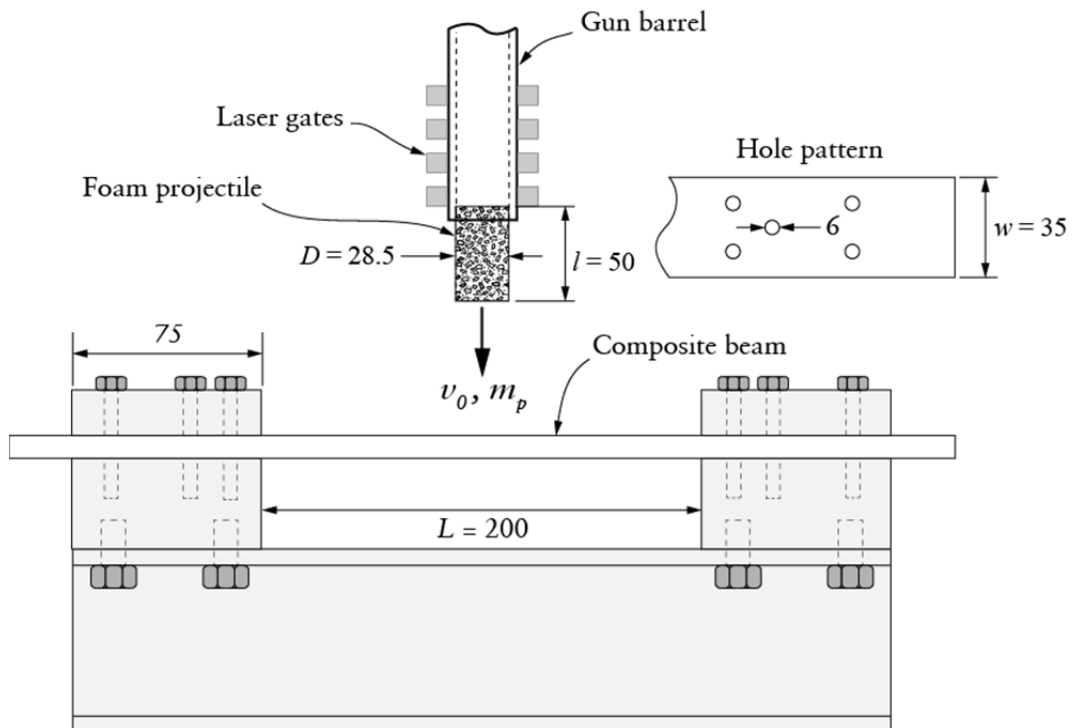


Fig. 11: Sketch of the setup used to impact the clamped beams by a metal foam projectile. All dimensions are in mm.



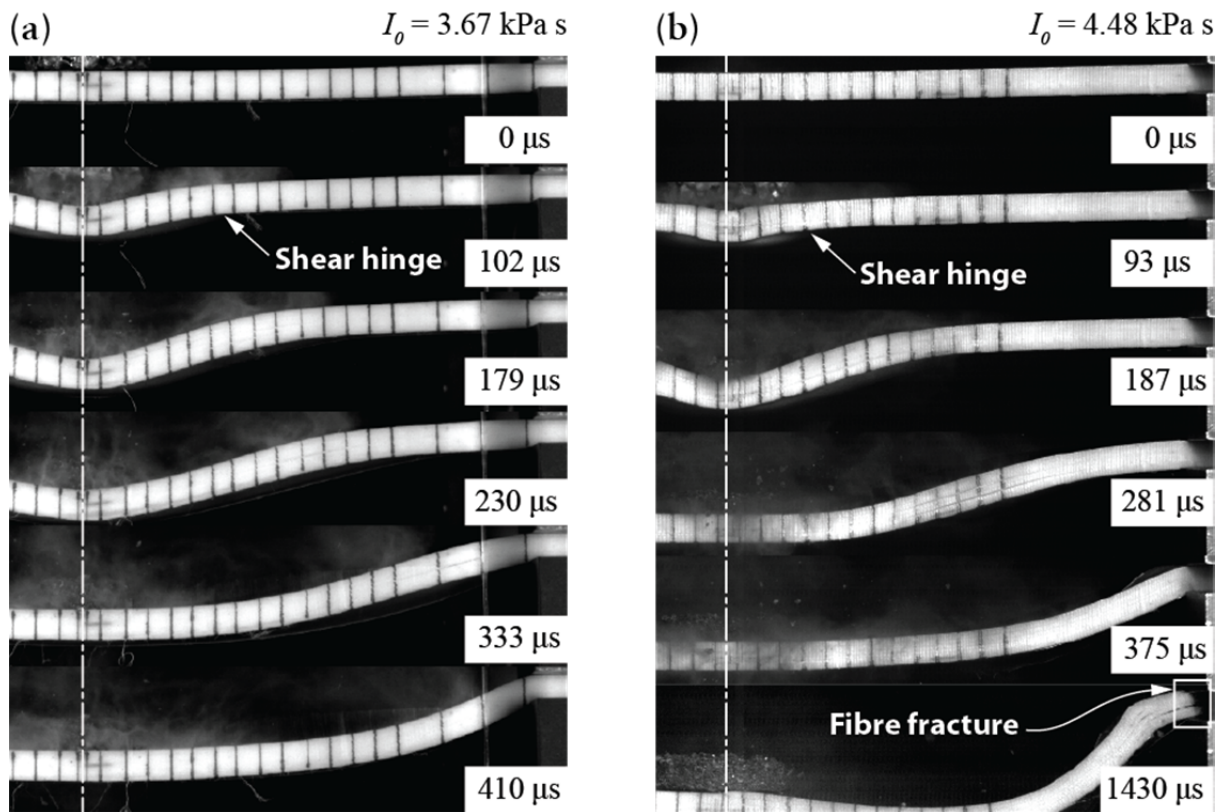


Fig. 12: Time sequence of high-speed images of the bolted HB26 beams subjected to two levels of impulse (a)  $I_0 = 3.67 \text{ kPa s}$ , for which ply fracture was not observed and (b)  $I_0 = 4.48 \text{ kPa s}$ , for which the beams fail and pull out from the supports. Time  $t$ , as measured after the instant of impact, is recoded on each image.



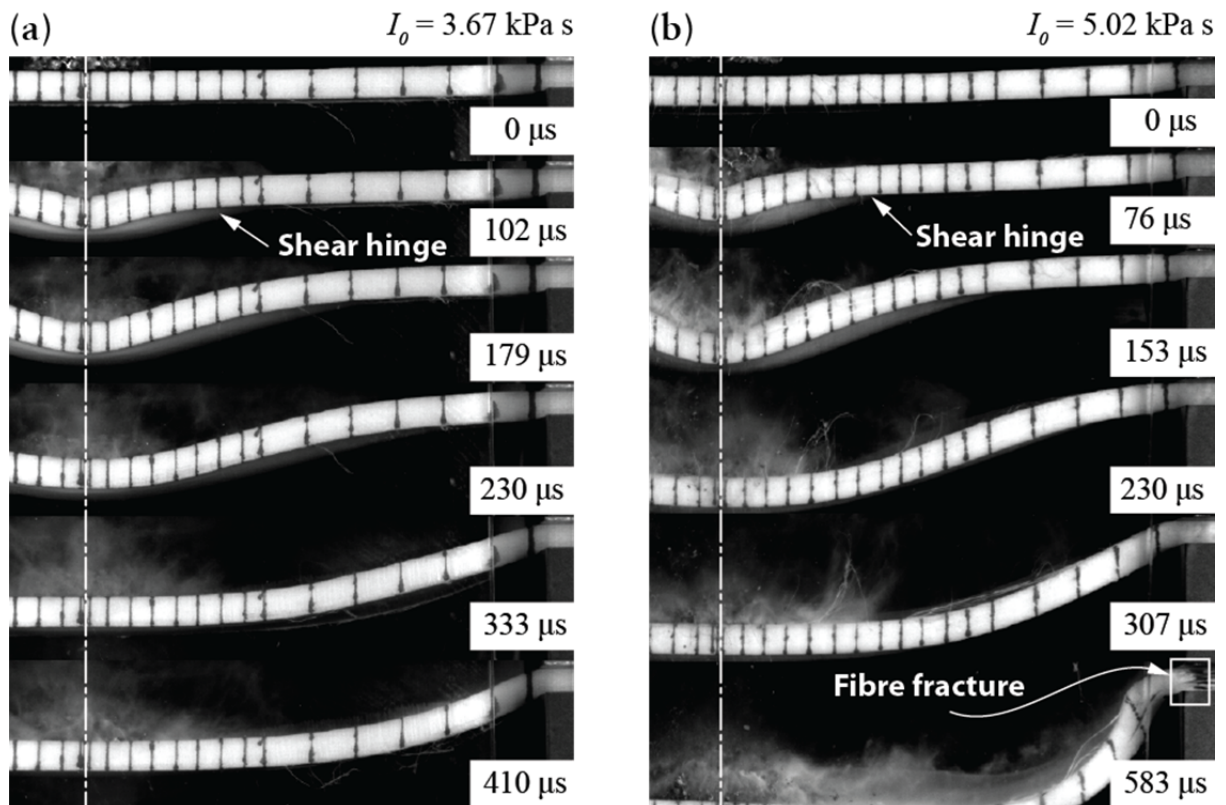


Fig. 13: Time sequence of high-speed images of the bolted HB50 beams subjected to two levels of impulse (a)  $I_0 = 3.67 \text{ kPa s}$  at which ply fracture was not observed and (b)  $I_0 = 5.02 \text{ kPa s}$  at which the beams fail and completely pull-out of the supports. Time  $t$ , as measured after the instant of impact, is recoded on each image.

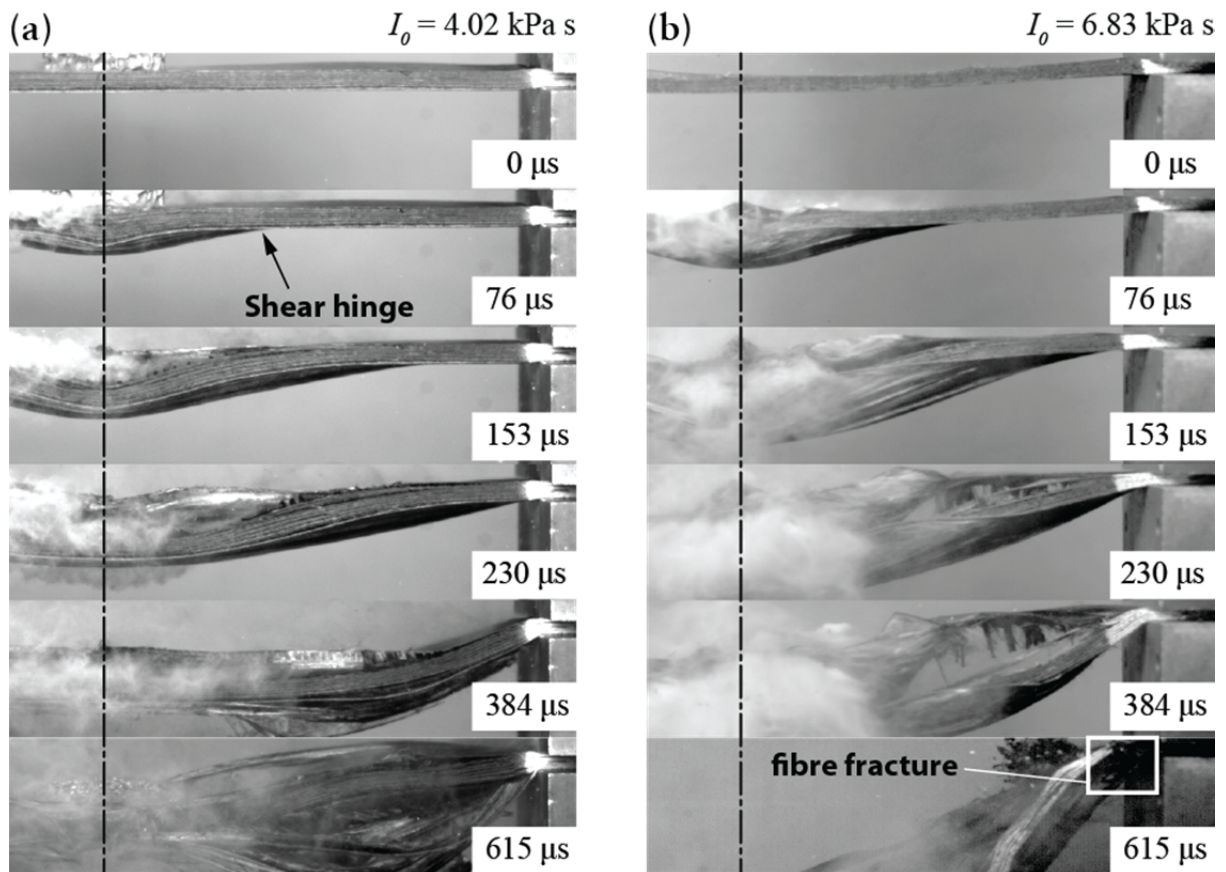


Fig. 14: Time sequence of high-speed images of the bolted CFRP-U beams subjected to two levels of impulse (a)  $I_0 = 4.02 \text{ kPa s}$  at which ply fracture was not observed and (b)  $I_0 = 6.83 \text{ kPa s}$  at which the beams fail and completely pull-out of the supports. Time  $t$ , as measured after the instant of impact, is recoded on each image.

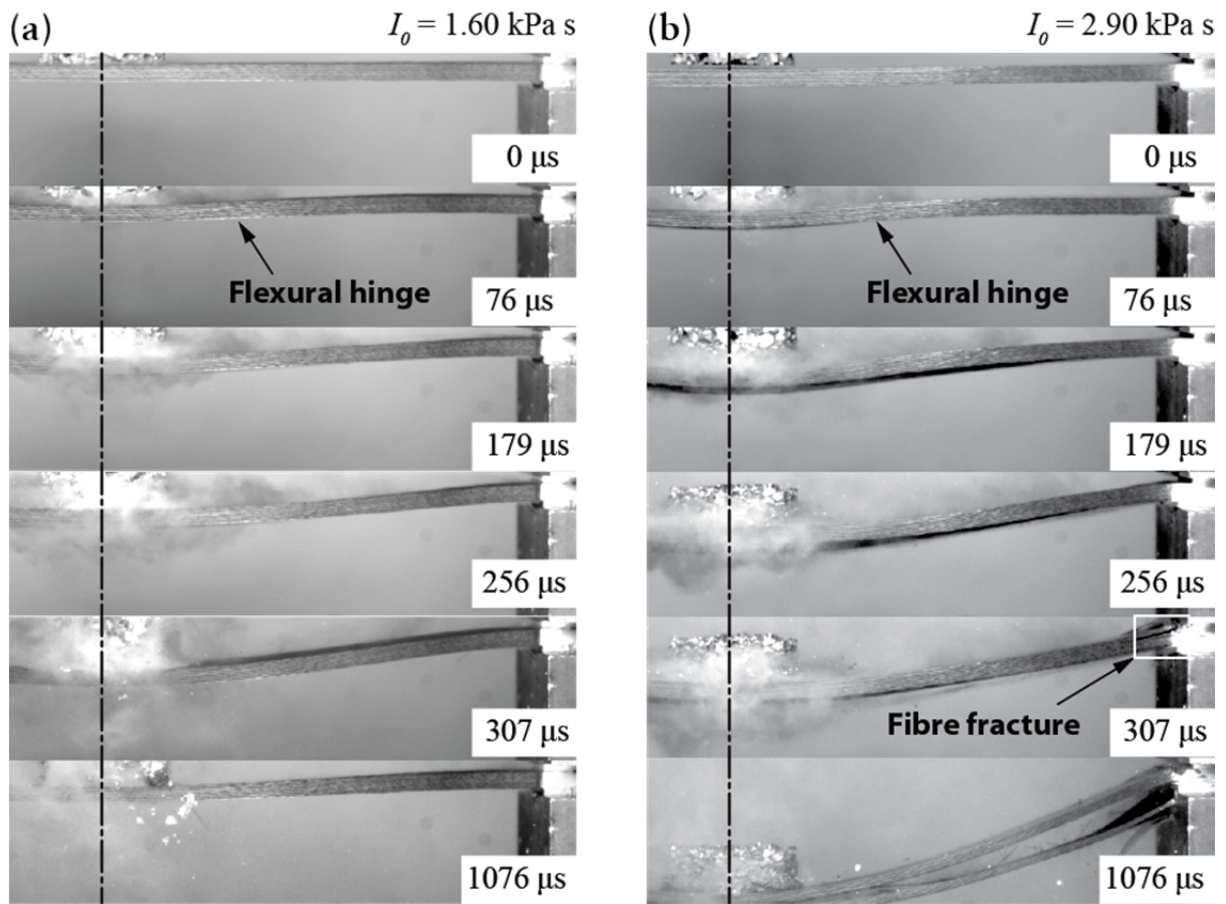


Fig. 15: Time sequence of high-speed images of the bolted CFRP-C beams subjected to two levels of impulse (a)  $I_0 = 1.60 \text{ kPa s}$  at which no damage was observed and (b)  $I_0 = 2.90 \text{ kPa s}$  at which the beams fracture across the full section, at the supports. Time  $t$ , as measured after the instant of impact, is recoded on each image.

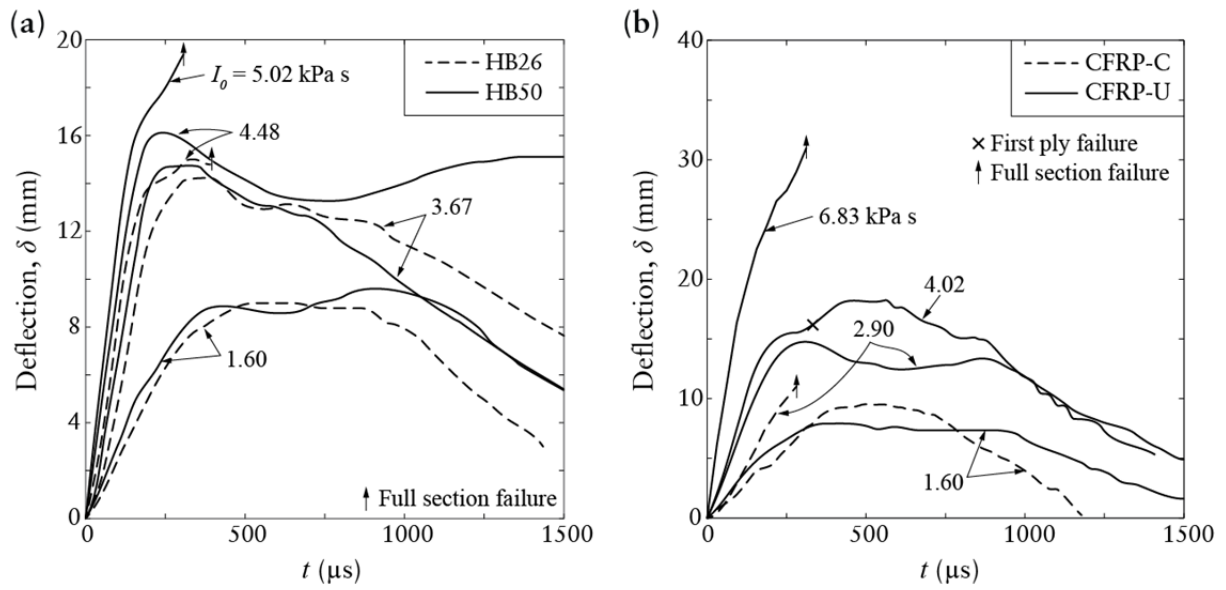


Fig. 16: Measured mid-span deflection  $\delta$  versus time  $t$  of (a) UHMWPE and (b) CFRP bolted beams. Time  $t = 0$  corresponds to the instant of impact.

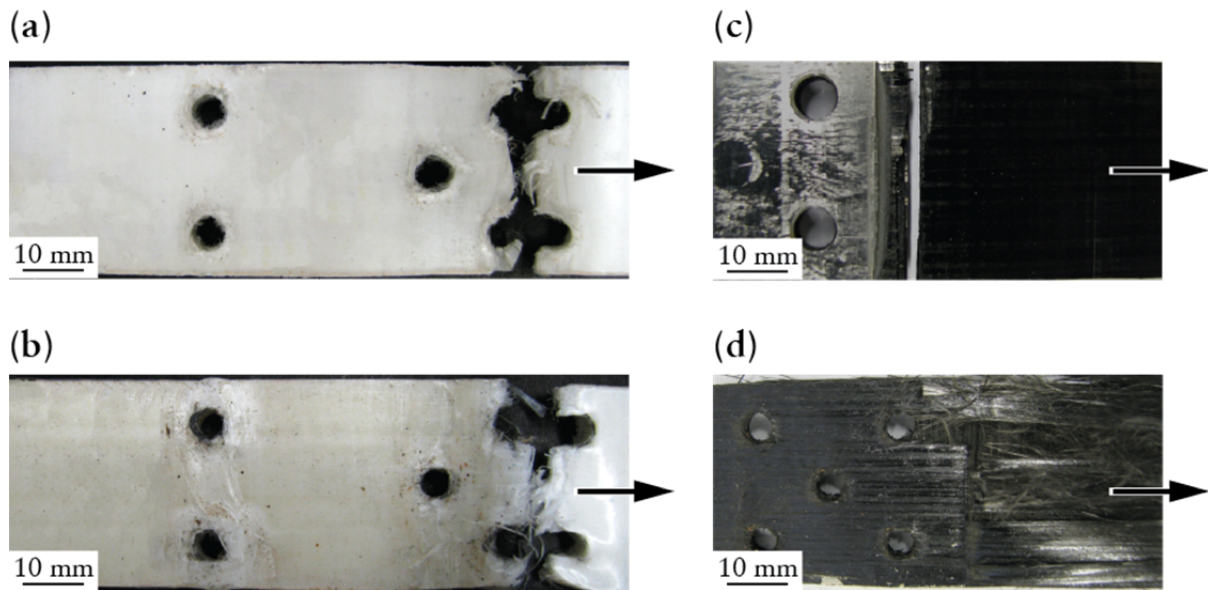


Fig. 17: Photographs of the failed ends of the bolted beams subject to the metal foam impact with impulses  $I_f$ . (a) HB26, (b) HB50, (c) CFRP-C and (d) CFRP-U.



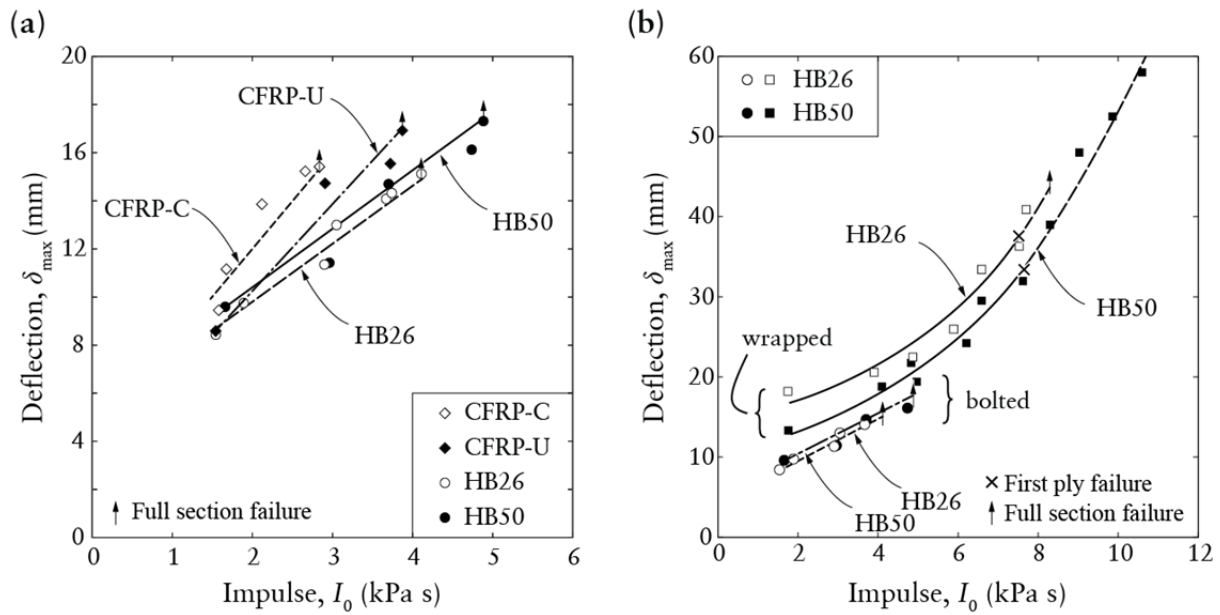


Fig. 18: The measured maximum deflections  $\delta_{\max}$  as a function of the projectile impulse  $I_0$  for the (a) four types of bolted beams and (b) the wrapped HB26 and HB50 beams. The deflections of the bolted HB26 and HB50 beams are included in (b).

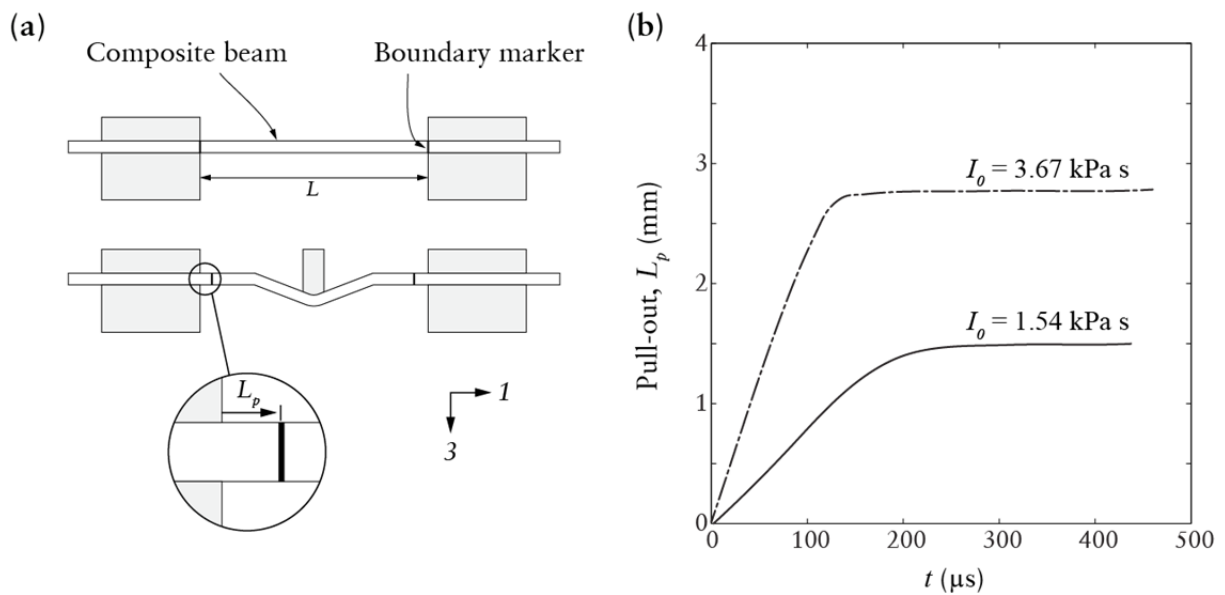


Fig. 19: (a) Sketch illustrating the measurement of pull-out using a marker at the clamped supports and (b) the measured pull-out  $L_p$  versus time  $t$  for the bolted HB26 beams subject to two selected values of the projectile impulse  $I_0$ . Time  $t = 0$  corresponds to the instant of impact.

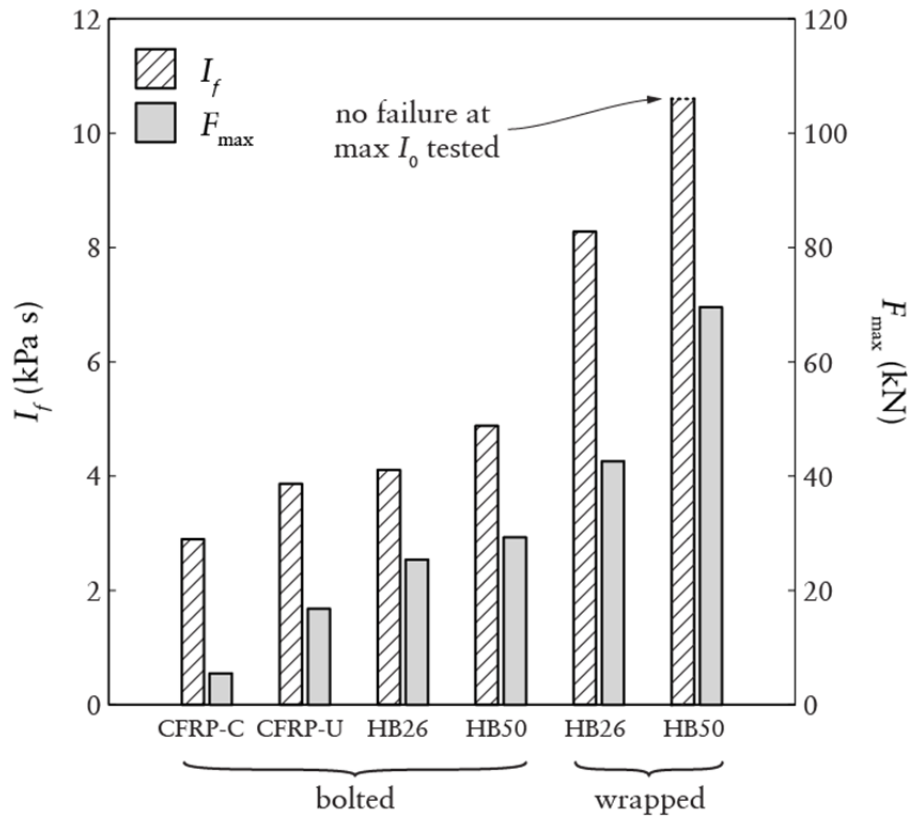


Fig. 20: A bar-chart illustrating the correspondence between the rankings of the beams in terms of the maximum force  $F_{max}$  in the quasi-static stretch-bend tests and the failure impulses  $I_f$  in the dynamic soft impact tests, for both the bolted and wrapped clamped beams.